

Magneto-optical Kerr-effect and magnetic anisotropy

Risalat Amir Khan and Niels Schröter

10th January 2012

Abstract

In the present report, we describe the measurement of the crystal anisotropy constant of an iron sample by obtaining hysteresis curves along the easy and hard crystal axis of the sample via the longitudinal magneto-optical Kerr-effect (MOKE). The constant was determined to $K_1 = (39 \pm 14) \frac{kJ}{m^3}$, which is in accordance with reference values. Furthermore, we measured the intensity contrast in dependence of the analyser angle and angle of incidence, thereby obtaining a Kerr angle of $\Phi_K = 0.075(9)deg$, which is in accordance with reference values. Unfortunately, the dependence of the contrast on the angle of incidence is only for p-polarized light consistent with reference data, not for s-polarized light. Finally, we obtained images of the domain-wall structure of a rare-earth iron garnet via Kerr-microscopy.

1 Theoretical background

1.1 Magneto-optical Kerr-effect

Linear polarized light that is reflected on a magnetized surface exhibits a rotation of the polarization with the angle Φ_K (Kerr rotation) and a ellipticity. This so called “Kerr effect” is caused by different absorption coefficients for left- and right-circular polarized light (n_-/n_+), since linear polarized light can be split into circular-polarized components. For an non-isotropic medium with small magnetic susceptibility, the Maxwell-equations result in an eigenvalue problem for the dielectric displacement field

$$\mathbf{D} = \underline{\epsilon}\mathbf{E} = \epsilon\mathbf{E} + i\epsilon Q\mathbf{m} \times \mathbf{E} \text{ with} \quad (1)$$

$$\underline{\epsilon} = \begin{pmatrix} \epsilon & \epsilon_{12} & \epsilon_{13} \\ -\epsilon_{12} & \epsilon & \epsilon_{23} \\ -\epsilon_{13} & -\epsilon_{23} & \epsilon \end{pmatrix} \text{ and } i\epsilon Q\mathbf{m} = \begin{pmatrix} \epsilon_{23} \\ -\epsilon_{13} \\ -\epsilon_{12} \end{pmatrix} \quad (2)$$

where $\underline{\epsilon}$ is the complex dielectric tensor, Q the Voigt constant (proportional to magnetization), \mathbf{m} the unit vector along the magnetization and \mathbf{E} the electric field [6]. The cross product in the second term represents the action of a Lorentz force, which motivates a semi-classical explanation of the Kerr effect: The incident light causes an oscillation of the electrons in the surface, but due to the Lorentz force, which is caused by the magnetization of the surface, the polarization of the resulting radiation is tilted. For light that is linearly polarized parallel to the x-axis, the Kerr angle takes the form [6]

$$\Phi_K \approx \tan \Phi_K = i \frac{n_+ - n_-}{n_+ n_- - 1} \approx i \frac{\sqrt{\epsilon} Q}{1 - \epsilon} \quad (3)$$

In relation to the measurement geometry, three forms of the Kerr-effect are distinguished [7]: (i) The *polar Kerr-effect* takes place in the case of a magnetization of the sample perpendicular to its surface. It is independent of the polarization of the incident light. (ii) The *transversal Kerr-effect* takes place when the magnetization is parallel to the sample surface (“in-plane”) and perpendicular to the plane of incidence. For those components of the light which are perpendicular to the plane of incidence, no rotation takes place. (iii) The *longitudinal Kerr-effect* takes place when the magnetization is in-plane and parallel to the plane of incidence and affects light with all forms of polarization.

1.2 Magnetic anisotropy

The magnetic anisotropy (density) U_K describes the contribution to the free energy of the Ferromagnet, which is dependent on the alignment of the magnetization. It consists of the so called *shape anisotropy*, which depends on the shape of the sample, and the *crystal anisotropy*, which describes energy differences for the magnetization along different crystal axis of the sample [2]. The latter can be described due to asymmetries in the overlap of electron distributions of neighbouring ions [5]: Because of spin-orbit interaction, the charge distribution is spheroidal and dependent of the direction of the electron spin. Thus, when the spins (and therefore the magnetization) are aligned along different axis in the crystal, the exchange energy and electrostatic interaction energy changes. Since iron has a cubic symmetry, the magnetic anisotropy can be expanded in powers of its direction cosines α_i , with $i = 1, 2, 3$. Because the opposite ends of a crystal axis are equivalent magnetically, uneven powers of α_i vanish and U_K must be invariant under interchanges of the α_i . Thus, expanding U_K to the sixth order gives [5]:

$$U_K \approx K_1(\alpha_1^2\alpha_2^2 + \alpha_2^2\alpha_3^2 + \alpha_3^2\alpha_1^2) + K_2(\alpha_1^2\alpha_2^2\alpha_3^2) \quad (4)$$

which vanishes for a magnetisation along the [100] axis (easy axis), since then $\alpha_1 = \alpha_3 = 0$, and is $\frac{K_1}{4}$ for a magnetization along [110] (hard axis), since then $\alpha_1 = \alpha_2 = \frac{1}{\sqrt{2}}$, $\alpha_3 = 0$.

1.3 Magnetic domains and hysteresis loops

In thermal equilibrium, the ground state of the magnetic moments in a ferromagnetic sample is usually a state of small domains with aligned moments, which is caused by the minimization of the stray field energy. The domain walls consist of rotating magnetic moments, they are called “Bloch walls” if their rotation axis is perpendicular to the domain walls, and “Néel walls” otherwise. [6]

When a weak external magnetic field is applied to the sample, the total magnetization rises by merely moving the boundaries between the domains to let one favourably orientated domains grow at the expense of unfavourably orientated ones (left inset in figure 1), in strong applied fields the domain magnetization rotates towards the direction of the field [5]. The average magnetization reaches a *saturation magnetization* M_s at comparably small fields with only one single domain orientation surviving. The domain type still prevails after the external field has been removed, resulting in a finite remaining magnetization called *remanence* M_r . To reach $M = 0$ again, one needs to reverse the magnetic field up to a value $-H_c$ which is called the *coercive field*. With increasing reversed magnetic field, another saturation magnetization at $-M_s$ is reached. In total one runs through a hysteresis loop which is shown in figure 1. The area of the hysteresis loop is the energy per volume required to move the boundaries between the domains through a full cycle. [4]

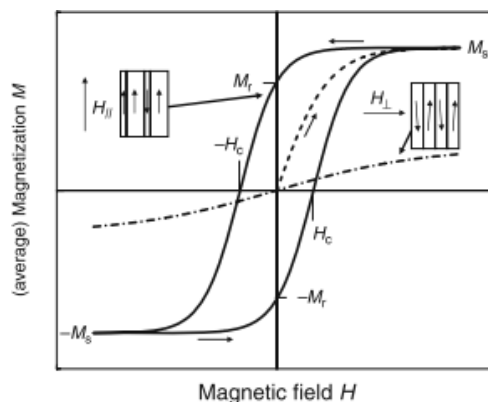


Figure 1: **Hysteresis loop** of a ferromagnet with single easy axis. *Dashed line*: initial magnetization starting from zero, H parallel to the easy axis. *Solid lines*: magnetization hysteresis, H parallel to easy axis. *Dash-dotted line*: H perpendicular to easy axis. Taken from Ref. [4].

From the hysteresis loops of iron along the easy and hard axes, one can obtain the anisotropy constant

K_1 by identifying the additional area in the [110] loop compared to the [100] loop as the anisotropy energy contribution $\frac{K_1}{4}$. The expected curves are shown in fig. 2.

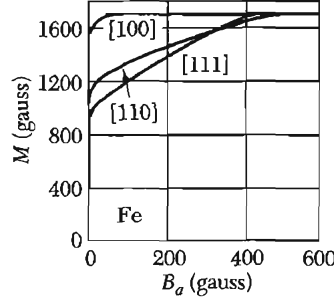


Figure 2: **Magnetization along different axis in Iron.** From the curves of iron we see that [100] has to be the easy axis, since its area of a hysteresis loop is smaller than the area of a loop with magnetizations along [110] and [111]. Taken from Ref. [5].

2 Experimental set-up

For the MOKE measurements, a linear polarized He-Ne laser is used as a light source. The beam is reflected on the iron-film sample under a well defined angle of incidence and passes through a rotatable polarization filter, which is used as an analyser. The intensity of the remaining light is measured by a photo-diode. The signal of the diode is amplified and recorded with a computer program. The external magnetic field applied to the sample is generated by a ring shaped iron core, which is wrapped by a coil. The sample is positioned within a slit in the ring, the magnetic field in the ring is proportional to the current applied in the coil.

2.1 Calibration of the magnetic field

The magnetic field in the slit can be calculated using Ampères law

$$N \cdot I = \int \mathbf{j} \cdot d\mathbf{A} = \int (\nabla \times \mathbf{H}) \cdot d\mathbf{A} = \int \mathbf{H} \cdot d\mathbf{s} = H_{core}s_{core} + H_{slit}s_{slit} \quad (5)$$

where N is the number of coil windings, I the current in the coil, \mathbf{j} the current density through the orientated surface \mathbf{A} , \mathbf{H} the magnetic field and $s_{core/slit}$ the length of the core and the slit, respectively. Due to the high permeability of the iron core, the first term can be neglected. With $H = B/\mu_0$, where B is the magnetic flux density and μ_0 the magnetic constant, one obtains for $N = 300$ and $s_{slit} = 12mm$

$$B_{slit} = \frac{N\mu_0}{s_{slit}} \cdot I \approx 31 \frac{mT}{A} \cdot I \quad (6)$$

We used a Hall-probe to obtain an experimental calibration of the field, measuring the magnetic flux density for different currents in the centre of the coil and at the prospective position of the sample. Using the the calibration of $1V \triangleq 100mT$ to convert the Hall-probe output to mT, we produced the calibration plots shown in fig. 3. Both curves show two branches which indicates the hysteresis of the iron core. We applied a linear fit to the lower branches in their linear range at about $[-3A, 3A]$. The slope of the curves gives a calibration factor of $31.73(3) \frac{mT}{A}$ for the centre position, which is in good agreement to the theoretical calculation, and $29.23(3) \frac{mT}{A}$ for the sample position. The error is solely taken from the spread of the data around the fit curve. It is small compared to other errors of the experiment and thus neglected in the following calculations. The difference in the calibration factors at different positions is mainly caused by the inhomogeneity of the field.

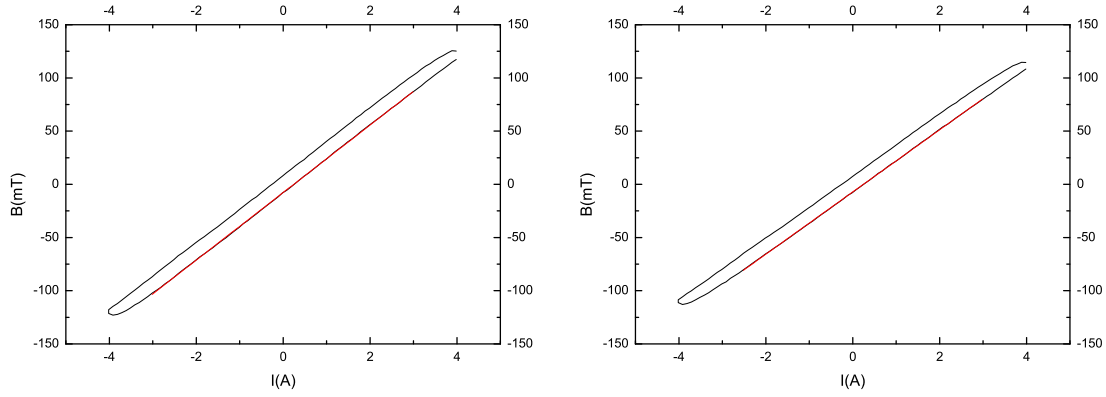


Figure 3: **Magnetic field calibration curves.** *Left:* Calibration at the centre of the coil. *Right:* Calibration at the sample position. Calibration data shown in black colour, linear fit in red colour. Both curves show two branches, indicating the hysteresis of the iron coil.

Triangle	Area in $10^{-3}T^2$	K_1 in $\frac{kJ}{m^3}$
upper left large triangle	17.8	56.8
upper left small triangle	11.1	35.3
lower right large triangle	12.2	38.8
lower right small triangle	6.2	24.8

Table 1: **Results of the numerical integration of the areas in fig. 4.** The conversion to the anisotropy constant is described in the text.

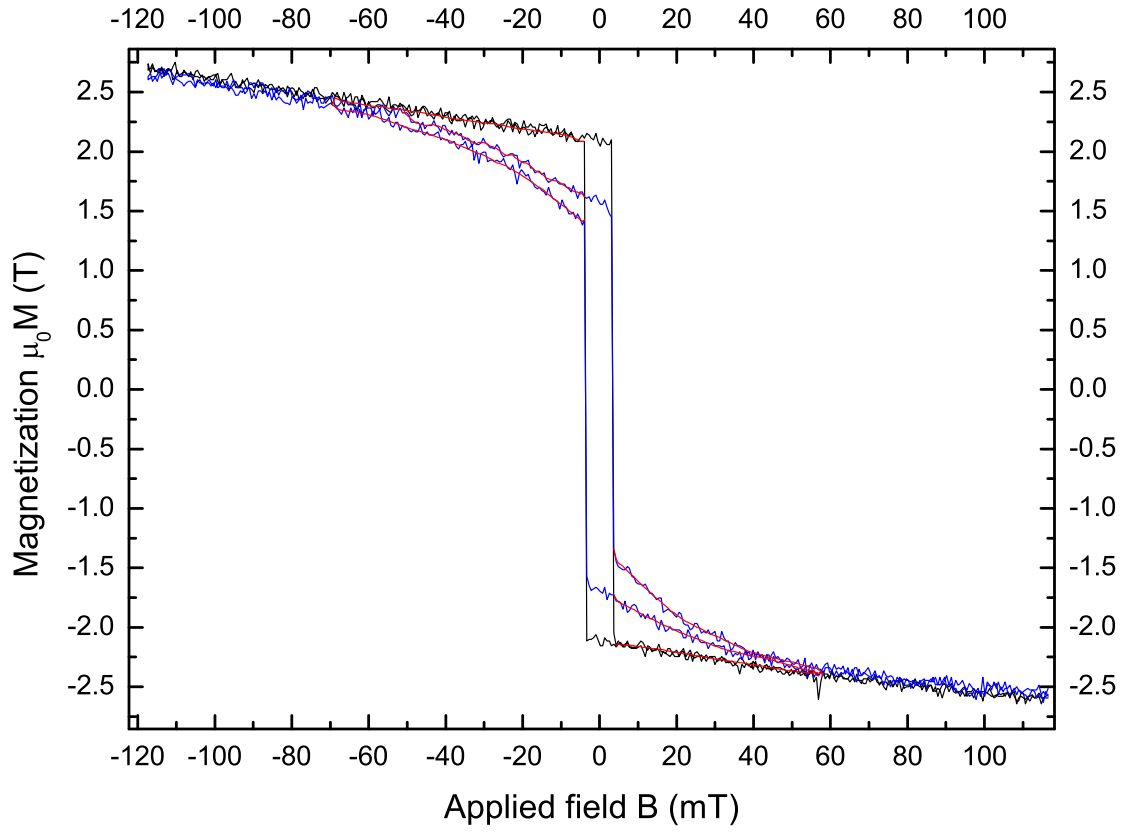
3 Results and Discussion

3.1 Anisotropy constant

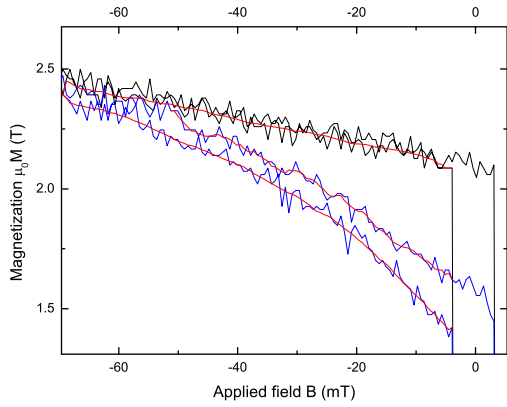
For the calculation of the anisotropy constant K_1 described in section 1.2 and 1.3, we superimposed the hysteresis curves taken with the MOKE set-up for the easy and hard axis orientation of the sample, which is shown in fig. 4. Because real systems usually show parts with different magnetization directions, p-polarized light (polarized parallel to the plane of incidence) would lead to a superposition of the transversal and longitudinal Kerr-effect [7]. Because the transversal Kerr-effect vanishes with s-polarized light (polarized perpendicular to the plane of incidence) as mentioned above, it is used for the measurement of the hysteresis curves shown below. The offset in the magnetization shown in both measurements is due to the remanence of the iron ring. For the calibration of the diode intensities, we used the saturation magnetization value given in the script as $\mu_0 M_S = 2.1T$. The magnetization shows a finite linear rise at the saturation level, which might be caused by the thermal drift of the magnetic moments [1]. We therefore estimated that saturation was reached for the easy axis at about the level of the offset magnetization. The error made in this calibration is due to the linear rise hard to quantify, but because we take the difference values between the hard-/easy-axis branches, which are probably equally affected by this distortion, it is presumably not very significant.

To obtain the anisotropy constant, we numerically integrated the area between the hard and easy axis, neglecting the offset caused by the remanence of the iron core. The four relevant triangles, two in the upper left and two in the lower right, are shown in fig. 4b and 4c, the numerical values for the area are tabulated in table 1.

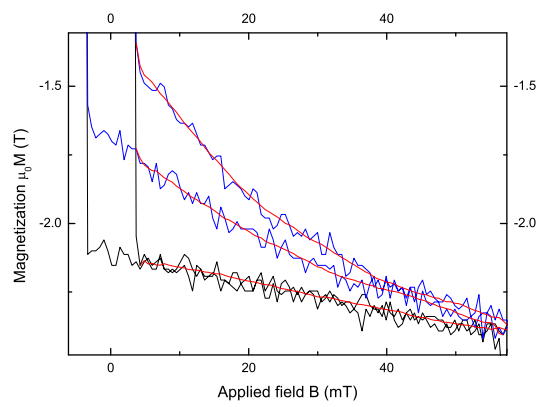
To convert the area A in energy densities and the crystal anisotropy constant, the following conversion



(a)



(b)



(c)

Figure 4: (a) **Hysteresis curves for hard (blue curve) and easy axis (black curve).** The remanence of the iron core leads to an offset of the magnetization. (b) shows the upper right part and (c) the lower left part of the curve shown in (a). The red lines indicate the triangles relevant for the determination of the anisotropy constant.

equation was applied

$$\frac{A}{\mu_0} = M \cdot B = \frac{K_1}{4} \quad (7)$$

where μ_0 is the magnetic constant. The areas of the triangles differ significantly, which might be caused due to inhomogeneities in the applied field or some other influence from the set-up [1]. Thus, we took the average value of the anisotropy constant as our result and the standard deviation from the average as an estimate for the error:

$$K_1 = (39 \pm 14) \frac{kJ}{m^3}$$

The result is within the error range identical with the reference value of $42 \frac{kJ}{m^3}$ given in Ref. [5], although in hindsight of the reference we acknowledge the results for the large upper left and small lower right triangle as outliers. This seems to be particularly likely, since they lie on a connected part of the hysteresis curve.

3.2 Kerr rotation

Because the Kerr rotation of the sample is expected to be very small ($\ll 1$ deg) we had to apply an indirect measurement technique. Hence, the reflected light from the sample was measured with an analyser at the position around the total distinction point, taking hysteresis curves for different positions of the analyser under an angle of incidence of 45 deg. From these, we calculated the corresponding contrast, defined as [2]

$$C(\alpha) = \left(\frac{I_+(\alpha) - I_-(\alpha)}{\frac{1}{2}(I_+(\alpha) + I_-(\alpha))} \right) \quad (8)$$

where $I_{+/-}$ are the signal intensities for the two opposed saturation magnetizations and α the angle of the polarizer. Since the equipment can only measure intensities up to a certain voltage, we had to apply an offset voltage which corresponds to an offset Intensity which extends eq. 8 to

$$C(\alpha) = \left(2 \frac{I_+(\alpha) - I_-(\alpha)}{I_+(\alpha) + I_-(\alpha) + 2I_{off}} \right) \quad (9)$$

The expected contrast can also be numerically obtained by modifying Malus Law

$$I(\alpha) = I_0 \cos^2(\alpha - \alpha_0) \quad (10)$$

where α_0 is the polarization of the incoming light to the analyser. Taking into account that we measure around the point of total distinction (phase-shift of $\frac{\pi}{2}$), light polarization is rotated after reflection by Φ_K and that even at the total extinction point there is some rest intensity I_1 due to imperfections in the analyser and the ellipticity of the reflected light, we used the following Ansatz [3]

$$I_{\pm}(\alpha) = I_0 \sin^2(\alpha - \alpha_0 \pm \Phi_K) + I_1 \quad (11)$$

Therefore, after linearising the sine function, eq. 8 becomes

$$C(\alpha) \approx \frac{4(\alpha - \alpha_0)\Phi_K}{(\alpha - \alpha_0)^2 + \Phi_K^2 + \frac{I_1}{I_0}} \quad (12)$$

The results of our Kerr angle measurements are shown in fig. 5 together with a fit of eq. 12. The errors in the intensity measurements were estimated from the noise at the saturation level. Because the contrast has to change its sign after going through the total distinction, we plotted the negative contrast for angles below the total distinction point. The results for the fit-parameters are shown in table 2, the errors are solely taken from the deviation of the data from the curve. As can be seen from the fit-curve and from the adjusted coefficient of determination R^2 , the model gives a satisfying description of the data, although there are deviations around the extremal points. This might be

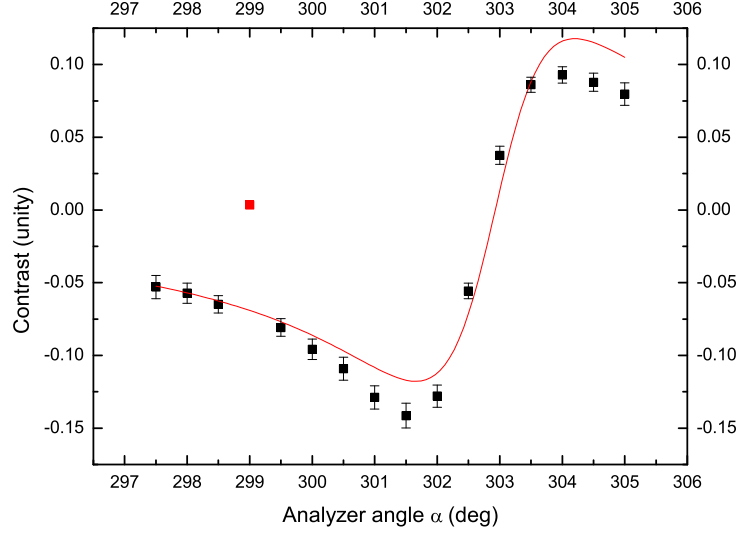


Figure 5: **Contrast dependence on the analyser angle.** The red point indicates an outlier. The red line represents a fit of equation 12, from which the Kerr angle was derived. The deviations of the fit around the extrema of the data is due to shortcomings in the model.

α_0/deg	Φ_K/deg	$\frac{I_1}{I_0}$	$Adj. R^2$
302.9(2)	0.075(9)	1.6(4)	0.953

Table 2: **Results from the fit of the data in fig. 5.**

caused by the approximations made to derive eq. 12 or other shortcomings of the model, particularly since the deviation of the data is symmetric. The obtained Kerr rotation of

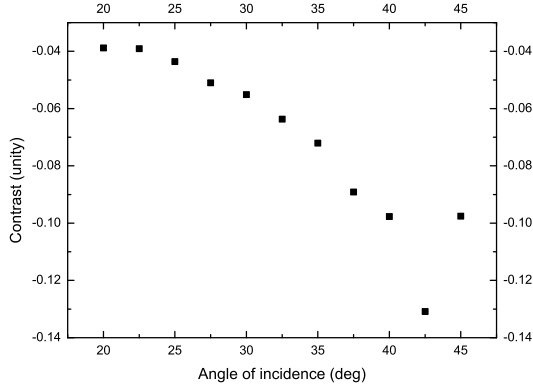
$$\Phi_K = 0.075(9)deg$$

is much smaller than 1 deg, as expected, but it was hard to find a concrete reference value for the Kerr rotation at the specific longitudinal configuration (e.g. we found no reference for this in the Landolt-Börnstein Database). From theoretically calculated graphs in Ref. [8] we extracted a Kerr rotation of $\Phi_{K-lit} \approx 0.05deg$, which is in good agreement with our results.

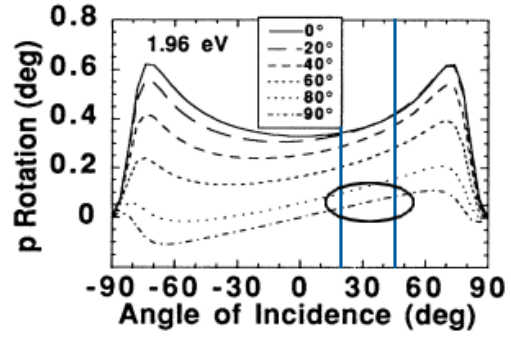
At a next step, we changed the angle of incidence from 45 to 20 deg at fixed analyser angle of $\alpha = 300deg$. Since the Kerr rotation is dependent on the incident angle, the contrast changes respectively. The results of our measurement for s- and p-polarization are shown in fig. 6, since we only want to derive qualitative conclusions, we neglected the error-bars, which would be in the order of the contrast-errors in fig. 5. As can be seen from eq. 12, the contrast is for this configuration negatively proportional to the Kerr rotation. Comparing our results qualitatively to the theoretical predictions from Ref. [8] as shown in fig. 6, we see that in p-polarization the contrast is decreasing with the angle of incidence in accordance with the theoretical rise of the Kerr rotation. In s-polarization, instead of an expected increase of the contrast with the angle of incidence, we see a decline of the contrast. The source of this error is hard to identify, because even if we did not apply the correct calibration to the incidence angles, the general tendency should be preserved. Thus, repeating the measurements would be appropriate to obtain further conclusions.

3.3 Kerr microscopy

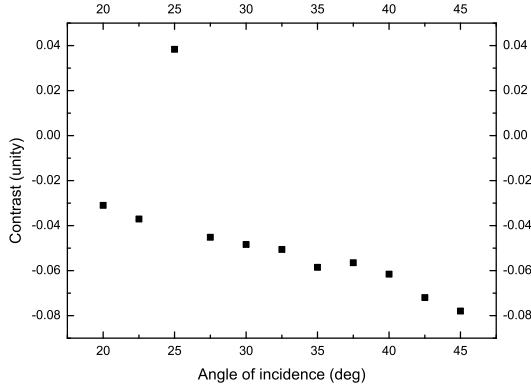
In a Kerr microscope, linearly polarized light is irradiated perpendicular to the sample surface and the reflected light passes an analyser before it is detected. Thus, magnetic domains which induce a Kerr rotation show a different intensity than those which leave the polarization of the incident light unaltered. Because of the perpendicular angle of incidence, the transversal and longitudinal Kerr effect



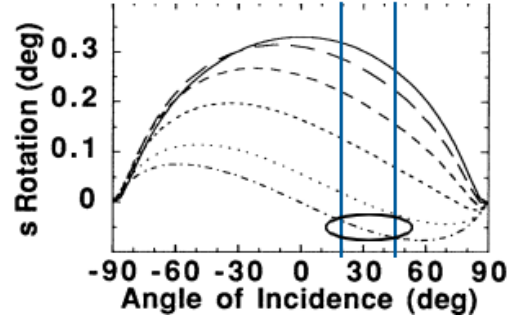
(a)



(b)



(c)



(d)

Figure 6: Contrast dependence on the angle of incidence. (a) and (c) show the results from our measurements for p- and s-polarized light, respectively, while (b) and (d), taken from Ref. [8], show the theoretical predictions. The contrast should be negative proportional to the Kerr rotation, thus the results for p-polarized light are in qualitative accordance to the predictions, while s-polarized light is not.

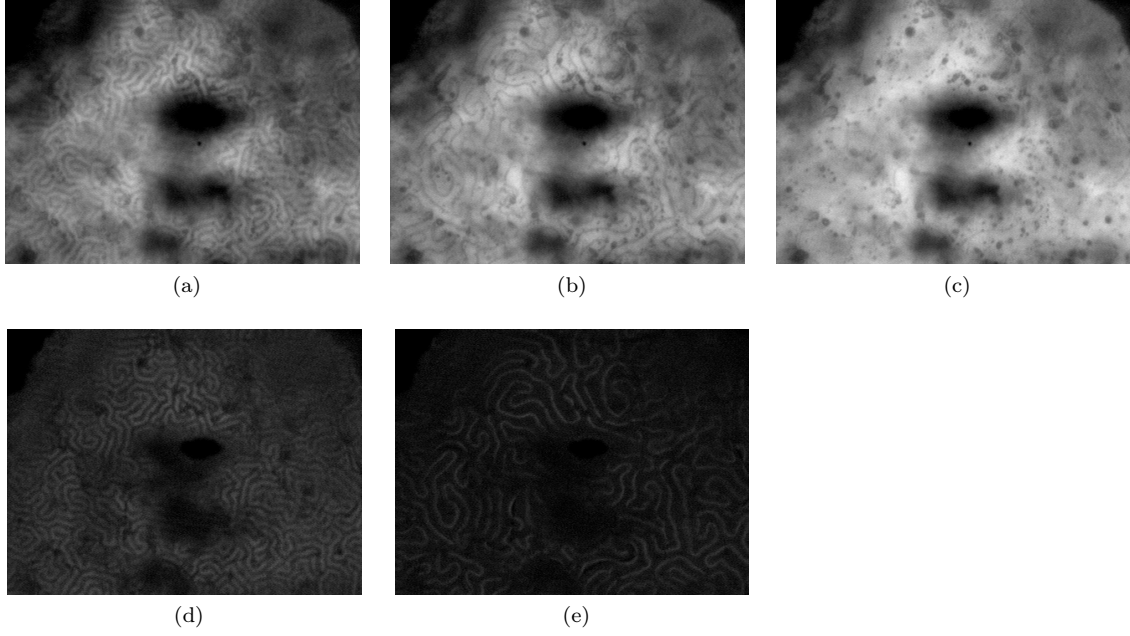


Figure 7: **Kerr-microscope image of rare-earth iron garnet.** (a) shows the remanence state, (b) the state at small applied field and (c) the single domain state at saturation. (d) and (e) show the difference images of (a) and (b) relative to (c), which allows for the better identification of the domain walls.

vanish [7] and only parts of the sample with magnetic components largely perpendicular to the sample surface lead to a Kerr rotation. In addition to the optical components of the set-up, an electromagnet is installed which generates a magnetic field which is approximately perpendicular to the sample surface. The strength and polarization of the field can be changed via the strength and polarization of the current through the coil of the electromagnet.

In the present experiment, a rare earth iron garnet is examined with the Kerr microscope set-up described above, which shows a maze pattern in the remanence state which can be altered by tuning the strength of the applied field. This process which is shown in fig. 7 with the images taken directly from the microscope camera. The pattern is characterised by small lines which start to disappear with higher fields until a saturation state with nearly no lines is reached, while the areas between the lines start to grow. The image of this saturation state can be used in a commonly applied technique to enhance the contrast of the domain state images by creating difference images while using the saturation state image as a reference. We used the program **ImageMagick** to exemplify this technique, the results of which are shown in fig. 7. Decreasing the magnetic field from the saturation state restored the maze-like pattern, though the structure itself was different compared to the one from the beginning, thus the formation of the observed lines appears to be a random process.

It is very instructive to note that at the inversion of the polarization of the applied field, the small lines inverted their contrast while the areas between them show only a slight change in contrast, which is shown in fig. 8. This behaviour allows the following interpretation of the observed phenomena: In the remanence state, the sample shows a domain structure with in-plane magnetization for the magnetic domains, which are separated by Bloch-domain-walls. I.e. the domain walls possess magnetization directions which have components that are largely perpendicular to the sample surface, which gives rise to the polar Kerr effect. Due to the resulting Kerr rotation, the domain walls show a different contrast than the domains themselves, where the transversal and longitudinal Kerr effect vanishes. Increasing the strength of the applied field leads to a growth of certain energetically preferred domains at the expense of others, thus to the reduction of the domain walls. The inversion of the applied field inverted the direction of the Bloch-wall-magnetization, thus leading to an inverted Kerr-rotation which gives rise to the inversion in the line contrast. Since the domains themselves show under both polarizations mainly an in-plane magnetization, the change in contrast is rather small (see fig. 8).

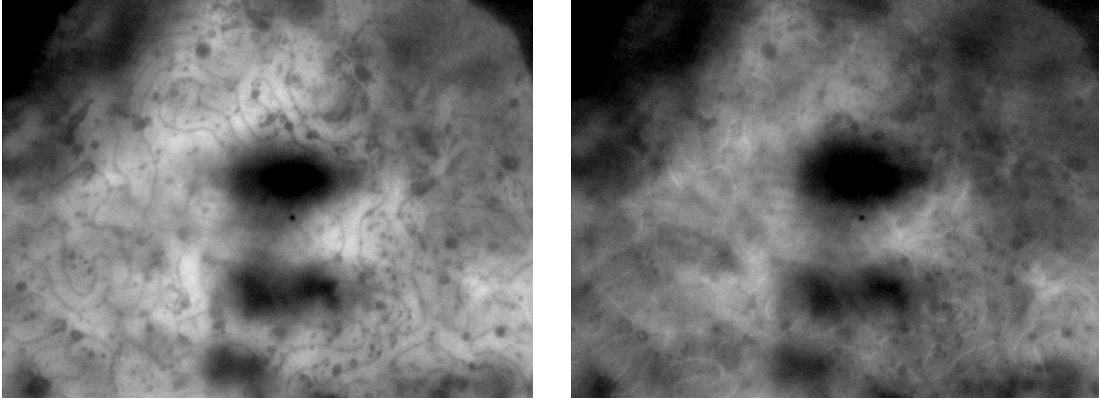


Figure 8: **Inversion of the external magnetic field direction.** *Left:* First type of coil current polarization. *Right:* Inverted coil current polarization. While the domain walls invert their contrast, the domains themselves show only a slight change in contrast. Thus, we conclude that the domains show mainly in-plane polarization while the domain walls are bloch walls with magnetization components largely perpendicular to the surface, giving rise to the polar Kerr-effect.

This interpretation of in-plane magnetization for iron films is in line with reference [7].

Another interesting effect was the apparent presence of a defect (e.g. atom vacancy), which lead to a pinning of a certain domain-wall to the defect, i.e. the line, once it was present, did not move when the applied field strength was changed.

References

- [1] *Talk given by S. Kreft and S. Sanchez in the Advanced Lab Seminar, FU Berlin, 2011.*
- [2] Freie Universität Berlin. *Script: Ma12: Magneto-optical Kerr-effect and magnetic anisotropy, Freie Universität Berlin.*
- [3] A. Hubert and R. Schäfer. *Magnetic domains: the analysis of magnetic microstructures.* Springer, 1998.
- [4] H. Ibach and H. Lüth. *Solid-State Physics.* Springer, 2009.
- [5] C. Kittel. *Introduction to solid state physics.* Wiley, 2004.
- [6] Gereon Meyer. *In situ Abbildung magnetischer Domänen in dünnen Filmen mit magnetooptischer Rasternahfeldmikroskopie.* PhD thesis, Freien Universität Berlin, 2003.
- [7] Birgit Vogelgesang. *Aufbau und inbetriebnahme eines hochauflösenden kerr-mikroskops und testmessungen an gdtb-, gdtbfe, fe- und feau- schichten.* Master’s thesis, Universität Kaiserslautern, 1997.
- [8] J. Zak, E. R. Moog, C. Liu, and S. D. Bader. Magneto-optics of multilayers with arbitrary magnetization directions. *Phys. Rev. B*, 43:6423–6429, Mar 1991.